University of Nebraska - Lincoln

DigitalCommons@University of Nebraska - Lincoln

Mechanical & Materials Engineering Faculty Publications

Mechanical & Materials Engineering, Department of

2017

Photoluminescence from Radiative Surface States and Excitons in Methylammonium Lead Bromide Perovskites

Dengyang Guo
Delft University of Technology

Davide Bartesaghi
Delft University of Technology

Haotong Wei
University of Nebraska-Lincoln

Eline M. Hutter
Delft University of Technology

Jinsong Huang
University of Nebraska-Lincoln, jhuang@unc.edu

See next page for additional authors

Follow this and additional works at: http://digitalcommons.unl.edu/mechengfacpub

🔵 Part of the Mechanics of Materials Commons, Nanoscience and Nanotechnology Commons, Other Engineering Science and Materials Commons, and the Other Mechanical Engineering Commons

Guo, Dengyang; Bartesaghi, Davide; Wei, Haotong; Hutter, Eline M.; Huang, Jinsong; and Savenije, Tom J., "Photoluminescence from Radiative Surface States and Excitons in Methylammonium Lead Bromide Perovskites" (2017). *Mechanical & Materials Engineering Faculty Publications*. 230.
http://digitalcommons.unl.edu/mechengfacpub/230

Authors

Dengyang Guo, Davide Bartesaghi, Haotong Wei, Eline M. Hutter, Jinsong Huang, and Tom J. Savenije

# Photoluminescence from Radiative Surface States and Excitons in Methylammonium Lead Bromide Perovskites

Dengyang Guo,[†] Davide Bartesaghi,[†] Haotong Wei,[‡] Eline M. Hutter,[†] Jinsong Huang,[‡] and Tom J. Savenije*,[†]

[†]Optoelectronic Materials Section, Department of Chemical Engineering, Delft University of Technology, 2628 HZ Delft, The Netherlands

[‡]Department of Mechanical and Materials Engineering and Nebraska Center for Materials and Nanoscience, University of Nebraska—Lincoln, Lincoln, Nebraska 68588-0656, United States

Ⓢ Supporting Information

ABSTRACT: In view of its band gap of 2.2 eV and its stability, methylammonium lead bromide ($MAPbBr_3$) is a possible candidate to serve as a light absorber in a subcell of a multijunction solar cell. Using complementary temperature-dependent time-resolved microwave conductance (TRMC) and photoluminescence (TRPL) measurements, we demonstrate that the exciton yield increases with lower temperature at the expense of the charge carrier generation yield. The low-energy emission at around 580 nm in the cubic phase and the second broad emission peak at 622 nm in the orthorhombic phase originate from radiative recombination of charges trapped in defects with mobile countercharges. We present a kinetic model describing both the decay in conductance as well as the slow ingrowth of the TRPL. Knowledge of defect states at the surface of various crystal phases is of interest to reach higher open-circuit voltages in $MAPbBr_3$-based cells.
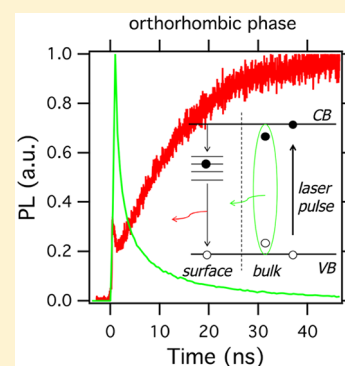
The past years have seen a huge increase in the power conversion efficiency of metal halide perovskite-based solar cells going from 3.8[1] to 22.1%.[2] The 2.2 eV band gap[3] makes methylammonium lead bromide ($MAPbBr_3$) a possible candidate to serve as a photoactive layer in a top cell of a multijunction solar cell.[4] The present record efficiency of a perovskite/Si tandem cell amounts to 23.6%(monolithic tandem)[5] and 26.4% (mechanically stacked tandem)[6] and is expected to reach efficiencies exceeding 30%. Open-circuit voltages[3,7−15] (V_{OC}) of 1.5 V[8,15] have been demonstrated for single-junction solar cells based on $MAPbBr_3$, and the best efficiency reported amounts to 11.4%.[10] However, this V_{OC} is still ~0.3 V lower than possible on the basis of its band gap.

Therefore, to transform $MAPbBr_3$ into a valuable solar energy material for a multijunction subcell, the photovoltaic properties should be improved. To this end, more insight into the generation and recombination dynamics of free charges in $MAPbBr_3$ is essential. From absorption spectra recorded at different temperatures,[14] an excitonic contribution has been observed throughout the three different crystal phases[16] of $MAPbBr_3$, for which an exciton binding energy (E_{ex}) of 40 meV was extracted.[17] However, a smaller E_{ex} of 15 meV is reported by Tilchin et al. obtained by microphotoluminescence.[18] In addition, $MAPbBr_3$ has also been studied by magneto-absorption,[19] yielding an E_{ex} of 25 meV.[20] Considering that these values are close to thermal energy at room temperature and somewhat larger than those reported for $MAPbI_3$[17,21] optical excitation might yield excitons at the cost of charge carriers. Temperature-dependent current−voltage character-

istics show that for the performance of solar cells based on $MAPbBr_3$ not only Shockley−Read−Hall (SRH) recombination but also surface recombination plays a crucial role.[9] Transient reflectance spectroscopy has been used to obtain the surface recombination velocity of $MAPbBr_3$, and the results suggest that the minimum domain size required to avoid the influence of surface recombination is 30 μm.[22] Hence, apart from losses due to exciton formation, SRH and surface recombination lead to rapid decay of charge carriers and are presumably the main reasons limiting the V_{OC} and hence the photovoltaic performance of $MAPbBr_3$-derived solar cells.[9,23]

So far, no specific research on the dynamics of mobile carrier generation in the three phases of $MAPbBr_3$ is performed. In this work, we carried out complementary temperature-dependent photoinduced time-resolved microwave conductance (TRMC) and time-resolved photoluminescence (TRPL) measurements. With TRMC, only excess free mobile charges are detected (for more details, see the SI), while TRPL yields information on both radiative recombination of free charges and radiative decay of excitons. Hence, the combination of TRMC and TRPL offers a full view on the generation and decay of excitons and charge carriers in $MAPbBr_3$. For our study, we selected $MAPbBr_3$ single crystals to eliminate the effects of grain boundaries and have a well-defined surface
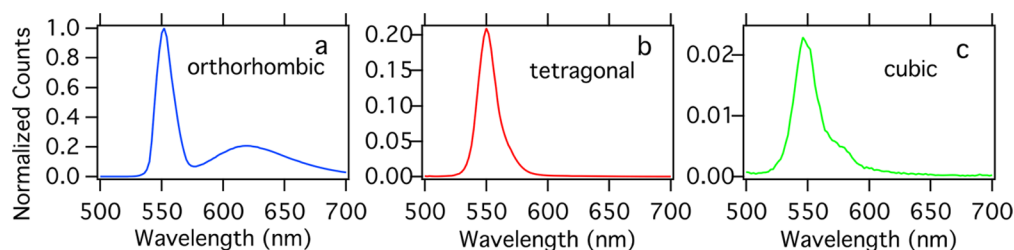
Figure 1. Photoluminescence (PL) emission spectra of a MAPbBr$_3$ single crystal recorded at (a) 77, (b) 170. and (c) 260 K. The PL spectrum of the orthorhombic phase was normalized to unity. Other spectra are scaled by the same factor.
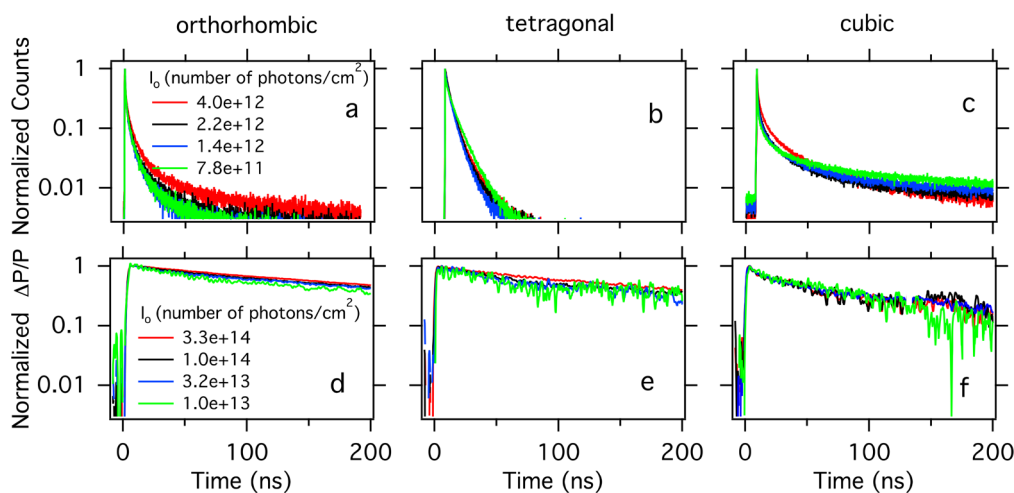

Figure 2. Upper panels: Normalized TRPL of MAPbBr$_3$ single crystals at 550 nm. Lower panels: To unity normalized photoconductance transients recorded at 500 nm. (a,d) Orthorhombic phase, T = 90 K; (b,e) tetragonal phase, T = 210 K; (c,f) cubic phase, T = 300 K.

instead.[22,24−27] From temperature-dependent single-crystal X-ray diffraction studies,[28] it is inferred that the transition from orthorhombic to tetragonal occurs at 144.5 K and that from tetragonal to cubic is at 236.9 K.[16,28] By combining information from TRPL and TRMC and additional modeling, we conclude that the low-energy emission in the cubic phase and that in the orthorhombic phase originate from radiative recombination of charges trapped at surface defects with mobile counter charges. From this work, it turns out that charges mainly decay via defect states, indicating that the wider band gap of MAPbBr$_3$ contains far more states in the forbidden band gap than MAPbI$_3$.

Single crystals of MAPbBr$_3$ were synthesized according to previously reported methods.[24] A crystal of around 5 × 3 × 2 mm^3 was mounted in a nitrogen-filled cryostat and illuminated using a pulsed excitation source at 405 nm. Emission spectra were recorded for different crystal phases at various indicated temperatures; see Figure 1. In the cubic crystal phase, the main PL peak at 548 nm is accompanied by a shoulder located at 580 nm, in line with previous reports.[29−31] However, even without the shoulder, the PL emission is asymmetric, indicating the presence of at least three components in the emission spectrum, in agreement with Fang et al.[32−34] This shoulder is not visible in the tetragonal phase. In the orthorhombic phase, two emission bands can be discerned: one at 550 nm and a second broad emission at about 620 nm. Note that even upon multiple cycles of heating and cooling this second emission peak at 620 nm emerges only in the orthorhombic phase, indicating that this feature is solely related to the orthorhombic phase. The position of the maximum of this second broad emission peak, however, changes from 618 nm at 77 K to 632

nm at 110 K. For thin MAPbBr$_3$ films, similar features are observed, although relative intensities differ (see SI Figure S1). This low-energy PL band has been observed before in metal halide perovskite films[35,36] and single crystals,[31] and surface defects are typically evoked to explain these typey of PL peaks.[31,35,37,38] It has been reported that the broader emission band was detected from a freshly cleaved single crystal and disappears after the crystal has been exposed to air,[31] and PL intensities and decay are subject to atmospheric conditions.[27] We should note that in our experiments the sample is measured and kept in a N$_2$ atmosphere at all times.

To further investigate the origin of the photoluminescence (PL), we measured the TRPL at the emission maximum of 550 nm, as shown in Figure 2a−c for the orthorhombic, tetragonal, and cubic crystal phases, respectively. The TRPL traces were measured at different indicated laser intensities. If the PL originates from second-order band-to-band recombination, a higher density will lead to an initially faster decay. However, although the excitation densities vary by almost a factor 10, the decay traces are on top of each other in the orthorhombic and tetragonal phases. In the cubic phase, the decay becomes slower upon increasing charge carrier densities, which is opposite to the trend expected for higher-order recombination. Consequently, for all three phases, it seems unlikely that the TRPL originates from second-order band-to-band recombination. Instead, we propose that the PL at 550 nm originates from first-order radiative decay of excitons, in line with previous results.[39]

To unravel the degree of exciton versus mobile charge carrier formation, we performed complementary TRMC measurements on the MAPbBr$_3$ single crystal. TRMC traces were

recorded for the three different crystal phases upon excitation at 500 nm, normalized to unity, and are shown in Figure 2d–f. (See SI Figure S2 for other temperatures.) Upon laser excitation, free mobile charges are generated, leading to a fast rise of the signal. The decay of the TRMC signal represents the reduction in the concentration of free charges by recombination and/or by immobilization in trap states. As can be observed for each phase, the TRPL decay is much faster than the TRMC decay. Besides, we see a large variation in PL decay kinetics throughout the three different phases, while this remains more or less identical in the TRMC signals. These observations suggest that the types of charge carriers responsible for the TRMC signal are not the same as those that give rise to the PL. Hence, this can be explained by assuming that part of the excitations yield excitons and only the remaining fraction is converted into free charges. To investigate how the charge carrier yield in this crystal is affected by temperature, we plotted the maximum of the photoconductance traces, which constitutes mobility and the yield of free charges (see SI eq 2) as a function of temperature and compare those to the trend of the mobility determined previously (see Figure 3).[40] From
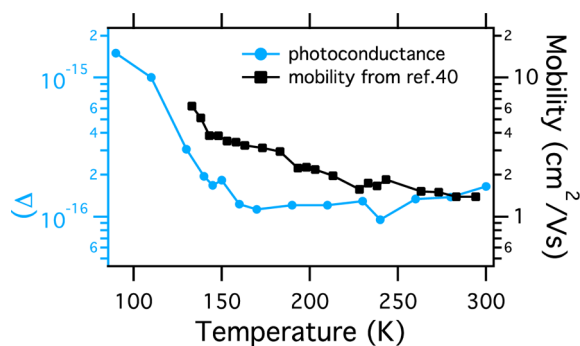

Figure 3. Maximum observed values of the photoconductance corrected for the incident number of photons ($I_0 = 2.8 \times 10^{12}/cm^2$) and sample area versus temperature. Left and right axes both cover 2 orders of magnitude to allow comparison. The excitation wavelength is 500 nm. The temperature-dependent mobility values measured by PR-TRMC are imported from the paper of Gélvez-Rueda et al.[40]

here, we can conclude that the charge carrier yield gradually decreases by approximately a factor 4 in the orthorhombic phase at 140 K in comparison with the yield at room temperature. Exciton binding energies between 15 and 40 meV reported for MAPbBr$_3$ could well explain this 4-fold reduction of the charge carrier yield. In addition, the increase in total PL yield with lowering temperatures, as shown in Figure 1, is in line with this. Finally, an increasing excitonic contribution in the absorption spectra of a thin film of MAPbBr$_3$ with lowering temperature agrees with our findings. (See SI Figure S3.)

Upon closer inspection of the TRMC data in Figure 2, we notice that the normalized TRMC traces recorded with different laser intensities are on top of each other, from which it is inferred that the recombination of free charges is (pseudo-)first-order. There are several explanations for this first-order recombination: in case the crystal is unintentionally doped, leading to a high concentration of background carriers, band-to-band recombination of excess carriers becomes pseudo-first-order. This process could lead to fast PL (as shown in Figure 2a–c) but should then also lead to fast recombination of free charges. Because this is in contrast with the long-lived TRMC signals (Figure 2d–f), fast radiative band-

to-band recombination with background carriers is unlikely. Alternatively, SRH recombination, enabled by states in the band gap or recombination by surface defects, might explain the first-order decay behavior. This is in contrast to previous research on MAPbI$_3$ single crystals, showing that light-induced carriers exhibit typical band-to-band second-order recombination.[41] Those results indicate that single crystals of MAPbI$_3$ contain fewer defect states than their bromide counterparts.

As shown in Figure 1a, the two emission bands in the orthorhombic phase are visible, having an energy difference of around 0.25 eV. The width of the emission at 622 nm suggests that it is not excitonic in nature but originates from a manifold of energy levels within the band gap. More specifically, in case the emission at 622 nm would be excitonic (with an exciton binding energy of 0.25 eV), this would imply that hardly any carriers would be generated upon photoexcitation at low temperatures, which is not the case. Interestingly, the TRPL decay at 622 nm is much slower than that at 550 nm (see Figure 4a). Upon combining the PL decay at 622 nm and the TRMC decay measured at corresponding excitation wavelengths and energies, we observe a substantial overlap, except for the first 50 ns. This similarity on longer time scales implies that the decay of the carriers as measured by TRMC and the radiative decay as detected by PL at 622 nm have most probably the same origin. Moreover, as shown in Figure 4b, the emission at 622 nm rises relatively slowly, extending over about 40 ns. Interestingly, this rise is slower than the PL decay at 550 nm. Hence, the emission at 622 nm cannot be explained by, for example, direct reabsorption of the emission at 550 nm.

To explain the similarity of the TRPL signal at 622 nm and the TRMC signal at 90 K, we suggest the following model depicted in Scheme 1. Upon optical excitation, a fraction of the absorbed photons generates mobile carriers, which directly contribute to the TRMC signal. Given the relatively high absorption coefficient[12,42] of the material at the excitation wavelengths used for both TRPL and TRMC, most of the charges are generated in proximity to the surface of the crystal. Surface states then act as a sink for conduction band electrons, which are rapidly trapped. We postulate that radiative recombination of these trapped electrons with mobile valence band holes leads to the broad 622 nm PL. We include in our model one-dimensional diffusion of charges.[32,34] Initially, the concentration gradient causes the diffusion of charges toward the bulk of the crystal. Depletion of both mobile electrons and holes in the region close to the surface causes local inversion of the concentration gradient, leading to diffusion of mobile charges from the bulk of the crystal toward the surface. The space- and time-dependent concentrations of free electrons (n_e), free holes (n_h), and trapped electrons (n_T) are described by a set of coupled differential equations

$$\frac{\partial n_e(x, t)}{\partial t} = D_e \frac{\partial^2 n_e(x, t)}{\partial x^2} + G(x, t) - k_{in}(x) n_e(x, t) \qquad (1)$$

$$\frac{\partial n_h(x, t)}{\partial t} = D_h \frac{\partial^2 n_h(x, t)}{\partial x^2} + G(x, t) - k_{TE}(x) n_h(x, t) n_T(x, t) \qquad (2)$$

$$\frac{\partial n_T(x, t)}{\partial t} = k_{in}(x) n_e(x, t) - k_{TE}(x) n_h(x, t) n_T(x, t) \qquad (3)$$

In this set of equations, x represents the distance from the surface. The generation rate of free charges, $G(x,t)$, is determined by the temporal profile and by the penetration
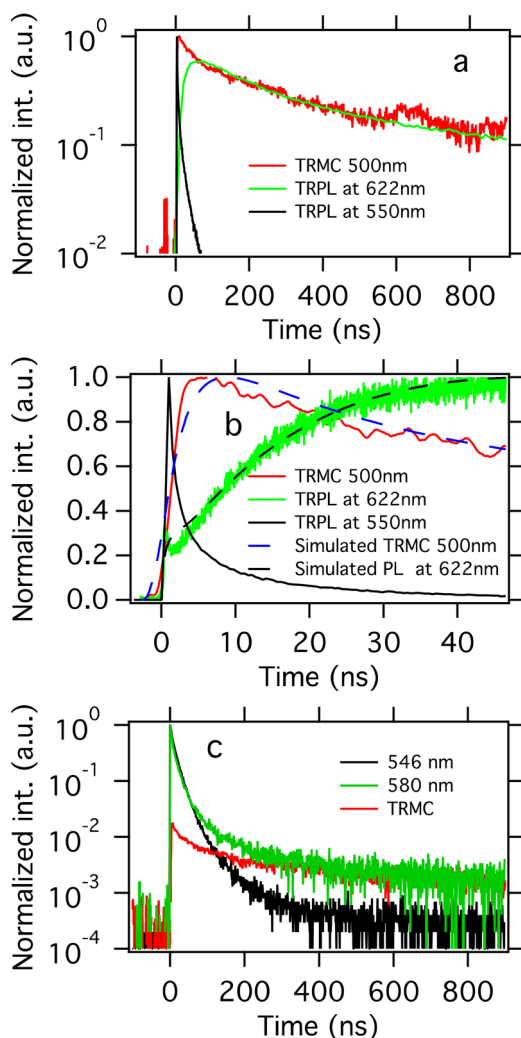
Figure 4. (a) Comparison of TRMC (red) and TRPL (green at 622 nm and black at 550 nm) signals at 90 K, orthorhombic phase. The TRMC trace is recorded using an excitation wavelength of 500 nm, while the excitation wavelength for the TRPL is 405 nm; the incident numbers of photons are 10^{13} and $4 \times 10^{12}/cm^2$, respectively. (b) Same traces as those in (a) on shorter time scales: note, the TRPL at 622 nm shows a slow 40 ns rise time. Dashed lines: calculated TRMC and TRPL by the model introduced in Scheme 1. (c) Comparison of TRMC (red) and TRPL (black at 546 nm and green at 580 nm) signals at 300 K, cubic phase.

depth of the laser pulse. As photorecycling efficiency in MAPbBr$_3$ single crystals is negligible (less than 0.5%),[33] we do not take this process into account. D_e and D_h are the diffusivities of electrons and holes derived from reported mobility values,[43] respectively. The trapping of free electrons at the surface and the recombination of free holes with trapped electrons are governed by the rate constants $k_{in}(x)$ and $k_{TE}(x)$, respectively. Assuming that the concentration of trap states in the region close to the surface is always much larger than the concentration of free electrons, the trapping rate depends only on the concentration of free electrons; the trapping process is therefore (pseudo-)first-order. On the contrary, the rate at which holes recombine with trapped electrons depends on the concentration of both species.

On the basis of the above kinetic model and using $k_{in} = 5 \times 10^9 \ s^{-1}$ and $k_{TE} = 1 \times 10^{-11} \ cm^{-3} \ s^{-1}$, we simulate the TRMC and TRPL traces, as shown in Figure 4b (see details in SI

Scheme 1. Proposed Kinetic Model for the Dynamics of Charges in the Orthorhombic Phase[a]
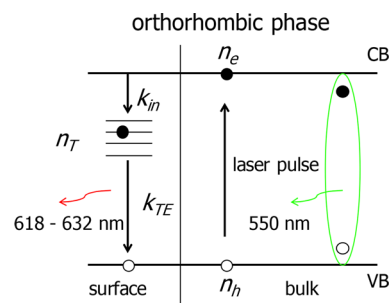
[a]Upon pulsed excitation, either excitons (green) or charges are formed. Electrons diffuse in all directions and are trapped at the surface with rate constant k_{in}. Trapped electrons, n_T, decay with rate constant k_{TE} back to the valence band by emitting a photon at ~622 nm. In principle, it is also possible that the reverse happens: Holes are trapped rapidly at the surface and decay with mobile conduction band electrons.

Simulation). The matching results suggest that due to the fast rate of trapping excited electrons are immobilized within a few nanoseconds from the laser pulse, leading to the fast initial decay of the TRMC trace. The slow rise of the PL signal at around 50 ns is the result of the slow recombination between holes and trapped electrons and the diffusion of charges toward the surface. Solving the system but neglecting the diffusional term does not yield such rise (see SI Figure S4), suggesting that diffusion is critical for the slow ingrowth. Unfortunately, neither from our measurements nor from the modeling can we exclude that hole traps instead of electron traps lead to the observed radiation.

Next, we could speculate if the shoulder of the emission band at 580 nm in the cubic phase is also due to radiative recombination of electrons trapped at the surface with valence band holes. Therefore, we measured the TRPL of the emission peak at 546 and 580 nm, shown in Figure 4c at 300 K. Interestingly, the PL decay at 580 nm shows a long tail, which is absent in the decay taken at 546 nm, in agreement with previous work.[39] On basis of the discussion above, we might argue that the fast reducing PL is due to the decaying excitons, while the tail might find its origin in luminescent decay of trapped electrons. Upon comparing the TRPL tail with the TRMC decay recorded in the cubic phase, a striking similarity is visible (see Figure 4c), which indicates that the PL at 580 nm of the PL spectrum of the cubic phase indeed originates from radiative decay of trapped charges. Although we could not discern a slow rise of the PL at 580 nm due to the low PL intensity, a recent paper shows that also here the PL exhibits a slow rise.[44] Obviously, for the tetragonal phase, there are no emissive surface defects, which could be ascribed to the fact that the trap states are above the conduction band edge or that the trapped electrons do not decay radiatively. From the results studied by density functional theory, along with photoemission and inverse photoemission spectroscopy,[45] these surface states could be ascribed to bromide vacancies or lead excess, as a result of MABr termination at the surface of MAPbBr$_3$. In view of the similar PL spectra that we observe for thin films and single crystals, we deduce that the same surface states are also present in thin MAPbBr$_3$ films and hence will also substantially affect the charge carrier dynamics. Because these states are

related to the surface, passivation might be a viable route to improve the open-circuit voltage.

In this work, we used complementary TRMC and TRPL to reveal the dynamics of photoexcited charges in the three crystal phases of a MAPbBr$_3$ single crystal. The conclusions are as follows: first, we find excitonic emission in each of the three phases, explaining the main emission band of the PL spectra at about 550 nm. From the TRMC measurements, we conclude that with lower temperature the charge carrier yield decreases by approximately a factor of 4. In contrast to higher-order band-to-band recombination observed in MAPbI$_3$ single crystals, in the present crystals, we observe mainly first-order decay, which occurs via defects. In the orthorhombic phase, electrons get quickly trapped by surface defects with disperse energy levels located about 0.25 eV below the conduction band. Radiative decay of these electrons with valence band holes leads to similar TRMC and PL lifetimes. Furthermore, in the orthorhombic phase, the TRPL shows a slow rise, extending over several tens of nanoseconds. This can be explained and modeled by the period involved with transport and trapping of charges to the surface by diffusion. A similar phenomenon could be present in the cubic phase, although the traps are much more shallow.

From this work, it turns out that charges mainly decay via defect states located at the surface, indicating that the wider band gap of MAPbBr$_3$ contains far more states in the forbidden band gap than MAPbI$_3$. As in both MAPbBr$_3$ single crystals and films surface states are governing the charge carrier dynamics, these surface states are expected to also play a crucial role in devices. Passivation of these surface states is a promising method to reach higher open-circuit voltages in MAPbBr$_3$-based cells.

ASSOCIATED CONTENT

Supporting Information

The Supporting Information is available free of charge on the ACS Publications website at DOI: 10.1021/acs.jpclett.7b01642.

Introduction of TRMC; complementary TRMC and calculation results; PL of thin films at the three phases; temperature-dependent transmission spectra; and experimental methods (PDF)

AUTHOR INFORMATION

Corresponding Author
*E-mail: T.J.Savenije@tudelft.nl.

ORCID
Davide Bartesaghi: 0000-0002-7467-269X
Eline M. Hutter: 0000-0002-5537-6545
Jinsong Huang: 0000-0002-0509-8778
Tom J. Savenije: 0000-0003-1435-9885

Notes
The authors declare no competing financial interest.

ACKNOWLEDGMENTS

REFERENCES

(1) Kojima, A.; Teshima, K.; Shirai, Y.; Miyasaka, T. Organometal Halide Perovskites as Visible-Light Sensitizers for Photovoltaic Cells. *J. Am. Chem. Soc.* **2009**, *131*, 6050−6051.

(2) National Renewable Energy Laboratory. *Research Cell Record Efficiency Chart.* https://www.nrel.gov/pv/assets/images/efficiency-chart.png (accessed Feb 20, 2017).

(3) Edri, E.; Kirmayer, S.; Cahen, D.; Hodes, G. High Open-Circuit Voltage Solar Cells Based on Organic-Inorganic Lead Bromide Perovskite. *J. Phys. Chem. Lett.* **2013**, *4*, 897−902.

(4) Polman, A.; Knight, M.; Garnett, E. C.; Ehrler, B.; Sinke, W. C. Photovoltaic Materials: Present Efficiencies and Future Challenges. *Science* **2016**, *352*, aad4424−aad4424.

(5) Bush, K. A.; Palmstrom, A. F.; Yu, Z. J.; Boccard, M.; Cheacharoen, R.; Mailoa, J. P.; McMeekin, D. P.; Hoye, R. L. Z.; Bailie, C. D.; Leijtens, T.; et al. 23.6%-Efficient Monolithic Perovskite/Silicon Tandem Solar Cells With Improved Stability. *Nat. Energy* **2017**, *2*, 17009.

(6) Duong, T.; Wu, Y.; Shen, H.; Peng, J.; Fu, X.; Jacobs, D.; Wang, E.; Kho, T. C.; Fong, K. C.; Stocks, M.; et al. Rubidium Multication Perovskite with Optimized Bandgap for Perovskite-Silicon Tandem with over 26% Efficiency. *Adv. Energy Mater.* **2017**, *7*, 1700228.

(7) Ryu, S.; Noh, J. H.; Jeon, N. J.; Chan Kim, Y.; Yang, W. S.; Seo, J.; Seok, S. Il. Voltage Output of Efficient Perovskite Solar Cells with High Open-Circuit Voltage and Fill Factor. *Energy Environ. Sci.* **2014**, *7*, 2614.

(8) Edri, E.; Kirmayer, S.; Kulbak, M.; Hodes, G.; Cahen, D. Chloride Inclusion and Hole Transport Material Doping to Improve Methyl Ammonium Lead Bromide Perovskite-Based High Open-Circuit Voltage Solar Cells. *J. Phys. Chem. Lett.* **2014**, *5*, 429−433.

(9) Zheng, X.; Chen, B.; Yang, M.; Wu, C.; Orler, B.; Moore, R. B.; Zhu, K.; Priya, S. The Controlling Mechanism for Potential Loss in CH$_3$NH$_3$PbBr$_3$ Hybrid Solar Cells. *ACS Energy Lett.* **2016**, *1*, 424−430.

(10) Mali, S. S.; Shim, C. S.; Hong, C. K. Highly Stable and Efficient Solid-State Solar Cells Based on Methylammonium Lead Bromide (CH3NH3PbBr3) Perovskite Quantum Dots. *NPG Asia Mater.* **2015**, *7*, e208.

(11) Heo, J. H.; Song, D. H.; Im, S. H. Planar CH3NH3PbBr3 Hybrid Solar Cells with 10.4% Power Conversion Efficiency, Fabricated by Controlled Crystallization in the Spin-Coating Process. *Adv. Mater.* **2014**, *26*, 8179−8183.

(12) Sheng, R.; Ho-Baillie, A.; Huang, S.; Chen, S.; Wen, X.; Hao, X.; Green, M. A. Methylammonium Lead Bromide Perovskite-Based Solar Cells by Vapor-Assisted Deposition. *J. Phys. Chem. C* **2015**, *119*, 3545−3549.

(13) Zhang, M.; Lyu, M.; Yu, H.; Yun, J. H.; Wang, Q.; Wang, L. Stable and Low-Cost Mesoscopic CH3NH3PbI2Br Perovskite Solar Cells by Using a Thin poly(3-Hexylthiophene) Layer as a Hole Transporter. *Chem. - Eur. J.* **2015**, *21*, 434−439.

(14) Chen, S.; Hou, Y.; Chen, H.; Richter, M.; Guo, F.; Kahmann, S.; Tang, X.; Stubhan, T.; Zhang, H.; Li, N.; et al. Exploring the Limiting Open-Circuit Voltage and the Voltage Loss Mechanism in Planar CH3NH3PbBr3 Perovskite Solar Cells. *Adv. Energy Mater.* **2016**, *6*, 1600132.

(15) Dymshits, A.; Rotem, A.; Etgar, L. High Voltage in Hole Conductor Free Organo Metal Halide Perovskite Solar Cells. *J. Mater. Chem. A* **2014**, *2*, 20776−20781.

(16) Chen, Q.; De Marco, N.; Yang, Y.; Song, T.-B.; Chen, C.-C.; Zhao, H.; Hong, Z.; Zhou, H.; Yang, Y. Under the Spotlight: The Organic-Inorganic Hybrid Halide Perovskite for Optoelectronic Applications. *Nano Today* **2015**, *10*, 355−396.

(17) Soufiani, A. M.; Huang, F.; Reece, P.; Sheng, R.; Ho-Baillie, A.; Green, M. A. Polaronic Exciton Binding Energy in Iodide and Bromide Organic-Inorganic Lead Halide Perovskites. *Appl. Phys. Lett.* **2015**, *107*, 231902.

(18) Tilchin, J.; Dirin, D. N.; Maikov, G. I.; Sashchiuk, A.; Kovalenko, M. V.; Lifshitz, E. Hydrogen-like Wannier-Mott Excitons in Single

Crystal of Methylammonium Lead Bromide Perovskite. *ACS Nano* **2016**, *10*, 6363−6371.

(19) Tanaka, K.; Takahashi, T.; Ban, T.; Kondo, T.; Uchida, K.; Miura, N. Comparative Study on the Excitons in Lead-Halide-Based Perovskite-Type Crystals CH3NH3PbBr3 CH3NH 3PbI3. *Solid State Commun.* **2003**, *127*, 619−623.

(20) Galkowski, K.; Mitioglu, A.; Miyata, A.; Plochocka, P.; Portugall, O.; Eperon, G. E.; Wang, J. T.-W.; Stergiopoulos, T.; Stranks, S. D.; Snaith, H. J.; et al. Determination of the Exciton Binding Energy and Effective Masses for the Methylammonium and Formamidinium Lead Tri-Halide Perovskite Family. *Energy Environ. Sci.* **2016**, *9*, 962−970.

(21) Sun, S.; Salim, T.; Mathews, N.; Duchamp, M.; Boothroyd, C.; Xing, G.; Sum, T. C.; Lam, Y. M. The Origin of High Efficiency in Low-Temperature Solution-Processable Bilayer Organometal Halide Hybrid Solar Cells. *Energy Environ. Sci.* **2014**, *7*, 399−407.

(22) Yang, Y.; Yan, Y.; Yang, M.; Choi, S.; Zhu, K.; Luther, J. M.; Beard, M. C. Low Surface Recombination Velocity in Solution-Grown CH3NH3PbBr3 Perovskite Single Crystal. *Nat. Commun.* **2015**, *6*, 7961.

(23) Yang, Y.; Yang, M.; Li, Z.; Crisp, R.; Zhu, K.; Beard, M. C. Comparison of Recombination Dynamics in CH3NH3PbBr3 and CH3NH3PbI3 Perovskite Films: Influence of Exciton Binding Energy. *J. Phys. Chem. Lett.* **2015**, *6*, 4688−4692.

(24) Fang, Y.; Dong, Q.; Shao, Y.; Yuan, Y.; Huang, J. Highly Narrowband Perovskite Single-Crystal Photodetectors Enabled by Surface-Charge Recombination. *Nat. Photonics* **2015**, *9*, 679−686.

(25) Shi, D.; Adinolfi, V.; Comin, R.; Yuan, M.; Alarousu, E.; Buin, A.; Chen, Y.; Hoogland, S.; Rothenberger, A.; Katsiev, K.; et al. Low Trap-State Density and Long Carrier Diffusion in Organolead Trihalide Perovskite Single Crystals. *Science* **2015**, *347*, 519−522.

(26) Saidaminov, M. I.; Abdelhady, A. L.; Murali, B.; Alarousu, E.; Burlakov, V. M.; Peng, W.; Dursun, I.; Wang, L.; He, Y.; Maculan, G.; et al. High-Quality Bulk Hybrid Perovskite Single Crystals within Minutes by Inverse Temperature Crystallization. *Nat. Commun.* **2015**, *6*, 7586.

(27) Fang, H.-H.; Adjokatse, S.; Wei, H.; Yang, J.; Blake, G. R.; Huang, J.; Even, J.; Loi, M. A. Ultrahigh Sensitivity of Methyl-ammonium Lead Tribromide Perovskite Single Crystals to Environ-mental Gases. *Sci. Adv.* **2016**, *2*, e1600534−e1600534.

(28) Stoumpos, C. C.; Malliakas, C. D.; Kanatzidis, M. G. Semiconducting Tin and Lead Iodide Perovskites with Organic Cations: Phase Transitions, High Mobilities, and near-Infrared Photoluminescent Properties. *Inorg. Chem.* **2013**, *52*, 9019−9038.

(29) Rao, H.-S.; Chen, B.-X.; Wang, X.-D.; Kuang, D.-B.; Su, C.-Y. A Micron-Scale Laminar MAPbBr3 Single Crystal for Efficient and Stable Perovskite Solar Cell. *Chem. Commun.* **2017**, *53*, 5163−5166.

(30) Kanemitsu, Y. Luminescence Spectroscopy of Lead-Halide Perovskites: Materials Properties and Application as Photovoltaic Devices. *J. Mater. Chem. C* **2017**, *5*, 3427−3437.

(31) Niesner, D.; Schuster, O.; Wilhelm, M.; Levchuk, I.; Osvet, A.; Shrestha, S.; Batentschuk, M.; Brabec, C.; Fauster, T. Temperature-Dependent Optical Spectra of Single-Crystal (CH3NH3)PbBr3 Cleaved in Ultrahigh Vacuum. *Phys. Rev. B: Condens. Matter Mater. Phys.* **2017**, *95*, 1−6.

(32) Yamada, T.; Yamada, Y.; Nishimura, H.; Nakaike, Y.; Wakamiya, A.; Murata, Y.; Kanemitsu, Y. Fast Free-Carrier Diffusion in CH$_3$NH$_3$PbBr$_3$ Single Crystals Revealed by Time-Resolved One- and Two-Photon Excitation Photoluminescence Spectroscopy. *Adv. Electron. Mater.* **2016**, *2*, 1500290.

(33) Fang, Y.; Wei, H.; Dong, Q.; Huang, J. Quantification of Re-Absorption and Re-Emission Processes to Determine Photon Recycling Efficiency in Perovskite Single Crystals. *Nat. Commun.* **2017**, *8*, 14417.

(34) Yamada, T.; Yamada, Y.; Nakaike, Y.; Wakamiya, A.; Kanemitsu, Y. Photon Emission and Reabsorption Processes in CH3NH3PbBr3 Single Crystals Revealed by Time-Resolved Two-Photon-Excitation Photoluminescence Microscopy. *Phys. Rev. Appl.* **2017**, *7*, 1−8.

(35) Priante, D.; Dursun, I.; Alias, M. S.; Shi, D.; Melnikov, V. A.; Ng, T. K.; Mohammed, O. F.; Bakr, O. M.; Ooi, B. S. The Recombination Mechanisms Leading to Amplified Spontaneous Emission at the True-Green Wavelength in CH3NH3PbBr3 Perovskites. *Appl. Phys. Lett.* **2015**, *106*, 081902.

(36) Motti, S. G.; Gandini, M.; Barker, A. J.; Ball, J. M.; Srimath Kandada, A. R.; Petrozza, A. Photoinduced Emissive Trap States in Lead Halide Perovskite Semiconductors. *ACS Energy Lett.* **2016**, *1*, 726−730.

(37) Dar, M. I.; Jacopin, G.; Meloni, S.; Mattoni, A.; Arora, N.; Boziki, A.; Zakeeruddin, S. M.; Rothlisberger, U.; Gra tzel, M. Origin of Unusual Bandgap Shift and Dual Emission in Organic-Inorganic Lead Halide Perovskites. *Sci. Adv.* **2016**, *2*, e1601156−e1601156.

(38) Fang, X.; Zhang, K.; Li, Y.; Yao, L.; Zhang, Y.; Wang, Y.; Zhai, W.; Tao, L.; Du, H.; Ran, G. Effect of Excess PbBr2 on Photoluminescence Spectra of CH3NH3PbBr3 Perovskite Particles at Room Temperature. *Appl. Phys. Lett.* **2016**, *108*, 071109.

(39) He, H.; Yu, Q.; Li, H.; Li, J.; Si, J.; Jin, Y.; Wang, N.; Wang, J.; He, J.; Wang, X.; et al. Exciton Localization in Solution-Processed Organolead Trihalide Perovskites. *Nat. Commun.* **2016**, *7*, 10896.

(40) Gélvez-Rueda, M.; Cao, D. H.; Patwardhan, S.; Renaud, N.; Stoumpos, C. C.; Schatz, G. C.; Hupp, J. T.; Farha, O. K.; Savenije, T. J.; Kanatzidis, M. G.; et al. Effect of Cation Rotation on Charge Dynamics in Hybrid Lead Halide Perovskites. *J. Phys. Chem. C* **2016**, *120*, 16577−16585.

(41) Bi, Y.; Hutter, E. M.; Fang, Y.; Dong, Q.; Huang, J.; Savenije, T. J. Charge Carrier Lifetimes Exceeding 15 Ms in Methylammonium Lead Iodide Single Crystals. *J. Phys. Chem. Lett.* **2016**, *7*, 923−928.

(42) Hoke, E. T.; Slotcavage, D. J.; Dohner, E. R.; Bowring, A. R.; Karunadasa, H. I.; McGehee, M. D. Reversible Photo-Induced Trap Formation in Mixed-Halide Hybrid Perovskites for Photovoltaics. *Chem. Sci.* **2015**, *6*, 613−617.

(43) Shi, D.; Adinolfi, V.; Comin, R.; Yuan, M.; Alarousu, E.; Buin, A.; Chen, Y.; Hoogland, S.; Rothenberger, A.; Katsiev, K.; et al. Low Trap-State Density and Long Carrier Diffusion in Organolead Trihalide Perovskite Single Crystals. *Science* **2015**, *347*, 519−522.

(44) Diab, H.; Arnold, C.; Ledee, F.; Trippe-Allard, G.; Delport, G.; Vilar, C.; Bretenaker, F.; Barjon, J.; Lauret, J.-S.; Deleporte, E.; et al. Impact of Reabsorption on the Emission Spectra and Recombination Dynamics of Hybrid Perovskite Single Crystals. *J. Phys. Chem. Lett.* **2017**, *8*, 2977−2983.

(45) Komesu, T.; Huang, X.; Paudel, T. R.; Losovyj, Y. B.; Zhang, X.; Schwier, E. F.; Kojima, Y.; Zheng, M.; Iwasawa, H.; Shimada, K.; et al. Surface Electronic Structure of Hybrid Organo Lead Bromide Perovskite Single Crystals. *J. Phys. Chem. C* **2016**, *120*, 21710−21715.

Photoluminescence from Radiative Surface States and Excitons in Methylammonium Lead Bromide Perovskites

Dengyang Guo,[1] Davide Bartesaghi,[1] Haotong Wei,[2] Eline M. Hutter,[1] Jinsong Huang,[2] and Tom J. Savenije[1*]

[1] Opto-electronic Materials Section, Department of Chemical Engineering, Delft University of Technology, 2628 HZ Delft, The Netherlands
[2] Department of Mechanical and Materials Engineering and Nebraska center for Materials and Nanoscience, University of Nebraska-Lincoln, Nebraska 68588-0656, USA

[*]Corresponding author: Tom J. Savenije: T.J.Savenije@tudelft.nl

Time-Resolved Microwave Conductivity (TRMC)

In TRMC we use laser pulses to excite a sample, a crystal in this study. The laser system is able to generate light of wavelengths from 240 nm to 2200 nm, and the light intensity can be tuned over 4 orders of magnitude. When microwaves pass through a sample containing mobile charges, the power of the microwaves decrease. The relationship between the normalized change in microwave power $\Delta P(t)/P$, the photoconductance ΔG, the mobility μ and the yield of free charges φ is given by equations (1) and (2):

$$\frac{\Delta P(t)}{P} = -k\Delta G(t) \qquad (1)$$

$$\frac{\Delta G_{max}}{I_0 \beta e F_A} = \varphi\left(\mu_h + \mu_e\right) \qquad (2)$$

where K is the so-called sensitivity factor, I_0 is the intensity of the laser in photons/pulse/unit area, F_A is the fraction of light absorbed at the excitation wavelength, β is a constant related to the inner dimensions of the waveguide. For crystals it is not straightforward to determine the K accurately. Therefore in this study TRMC data are expressed in $\Delta P(t)/(PI_0A)$, which is still proportional to the product of the yield of free charges, φ and the mobility, μ.
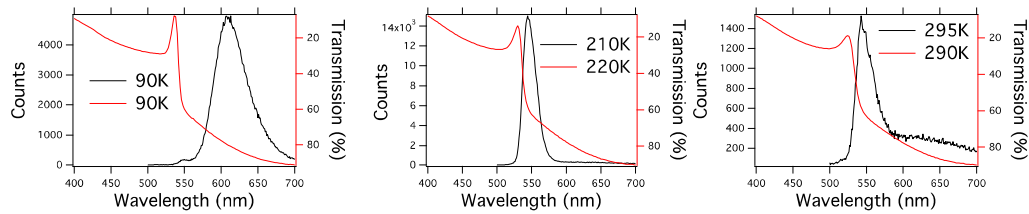

Fig. S1. PL and transmission spectra of the MAPbBr$_3$ thin films recorded at different temperatures. The films are made by methods shown below in Experimental methods.
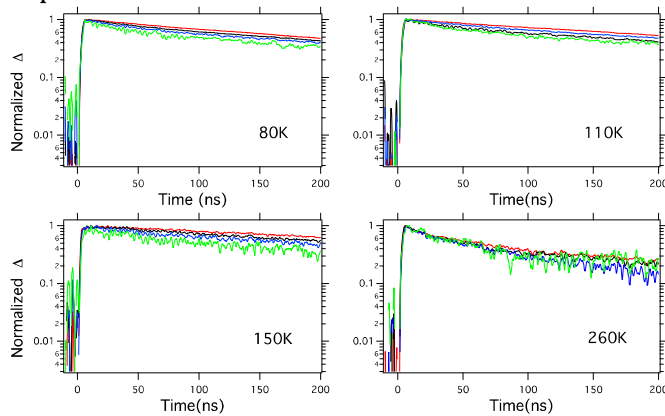

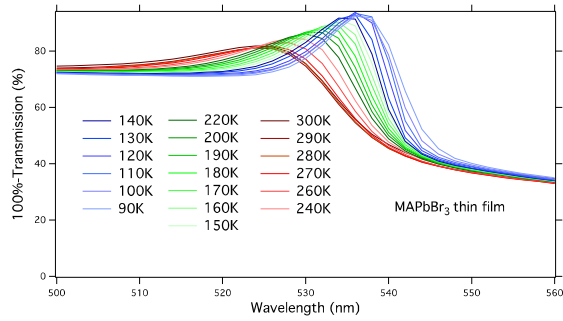**Fig. S2.** TRMC traces recorded at 500 nm at other temperatures.

Fig. S3. The temperature dependent transmission spectra of MAPbBr$_3$ thin film. The three colour series represent the three phases: red is for cubic phase, green is for tetragonal phase, and blue is for orthorhombic phase.
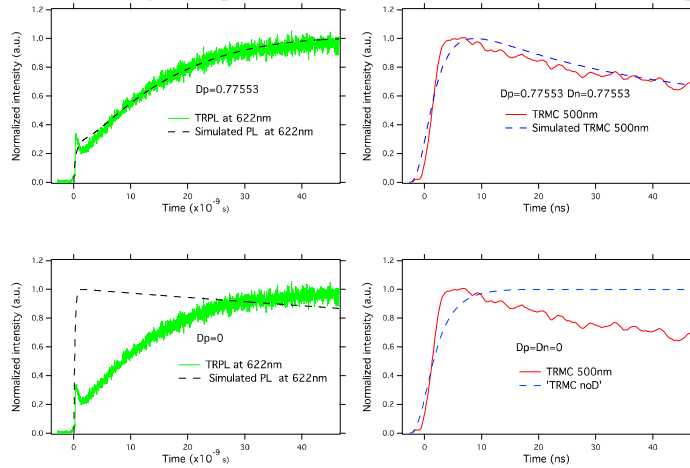

Fig. S4. Upper panels: Red: calculated, Black: experiments. The experimental PL data was smooth fitted before normalizing them. Lower panels: The simulation results from D = 0.
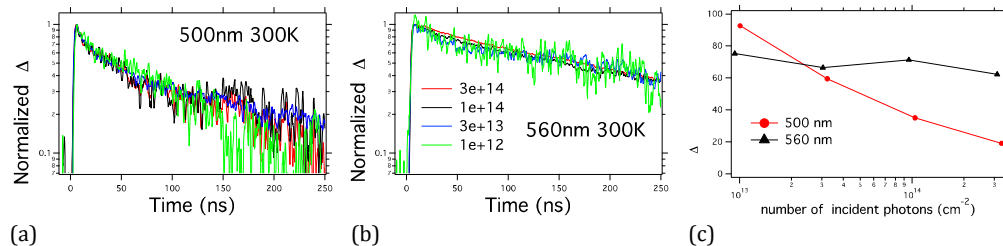

Fig. S5 Normalized ΔP/P, recorded at 300k illuminated at 500 nm laser (a) and 560 nm laser (b) of different intensities, distinguished by colours. (c) Maxima of ΔP/P divided by incident number of photons per sample area.

In Fig. S5c the maxima of ΔP/P divided by incident number of photons per sample area are plotted versus the incident number of photons. As shown the maximum values at 560 nm are almost constant, while those at 500 nm decrease with increasing intensities. An obvious explanation would be the presence of second order band-to-band recombination occurring at high densities. However, this seems in conflict with the fact that the TRMC traces follow first order kinetics as presented above. Obviously, at short timescales faster than we can resolve using the present technique, other processes occur which lower the charge carrier concentration yield on higher intensities. We suggest that apart

S3

from charges also excitons might be formed on optical excitation of MAPbBr3. According to the Saha equation the ratio of free charges, x reduces as the concentration of excitations, n in the MAPbBr3 single crystal significantly increases, while at the same time the yield of excitons increases. At 560 nm the excitation density is always over 1000 times lower than at 500 nm, leading at all intensities to a yield of charge carriers close to 1.

Experimental methods

Materials. Lead bromide (PbBr$_2$) (>98%, Sigma-Aldrich), Methylamine (CH$_3$NH$_2$) (40% w/w aq. soln., Alfa Aesar), Hydrobromic acid (HBr) (48% w/w aq. soln., Alfa Aesar), *N,N*-Dimethylformamide (DMF) (>99.8%, Alfa Aesar), Dichloromethane (DCM) (99.7%, , Alfa Aesar), Dimethyl sulfoxide (DMSO) (>99.9%, Sigma-Aldrich).

Synthesis of Methylammonium bromide (MABr). MABr was prepared by slowly mixing methylamine with HBr in 1:1 molar ratio under continuous stirring at 0 °C for 2 h. MABr was then crystallized by removing the solvent from an evaporator, washing three times in diethyl ether, and filtering the precipitate. The white crystal was obtained by recrystallization with ethanol, then dried in vacuum for 24 h, and kept in a dark and dry environment for further use.

Growth of MAPbBr$_3$ single crystal (SC). 1.5 M PbBr$_2$ and 1.5 M MABr were dissolved into DMF solution in a vial to keep the molar ratio of PbBr$_2$ to MABr is 1. Then the solution was heated on a hot plate. Finally, MAPbBr$_3$ SC can slowly grow by gradually increasing the temperature of the hot plate.

Fabrication of MAPbBr$_3$ thin film. The MAPbBr$_3$ thin film was spun coated on a quartz substrate by the anti-solvent method, and the spin coating process was conducted in glovebox with oxygen level lower than 100 particles per million. The perovskite precursor solution composed of PbBr$_2$ and MABr (1:1, in molar) was dissolved in mixed solvent (DMF: DMSO = 9:1, v/v). Then 80 μL precursor solution was spun onto substrate at 2000 rpm for 2 s and 4000 rpm for 60 s, the sample was quickly washed with 120 μL toluene at the 20th second of the 4000 rpm spin-coating. Subsequently, the sample was annealed at 70 °C for 10 min and 100 °C for 10 min.

Photoluminescence (PL) measurements of MAPbBr$_3$ single crystal. We used an Edinburgh LifeSpec spectrometer equipped with a single photon counter to measure PL spectra and lifetimes. An Oxford cryostat was installed in the LifeSpec measuring chamber, and the sample was kept all the time in the inner chamber of the cryostat.

Simulation

The differential equations proposed by the model in Scheme 1 are:

$$\frac{\partial n_e(x,t)}{\partial t} = D_e \frac{\partial^2 n_e(x,t)}{\partial x^2} + G(x,t) - k_{in}(x)n_e(x,t) \tag{1}$$

$$\frac{\partial n_h(x,t)}{\partial t} = D_h \frac{\partial^2 n_h(x,t)}{\partial x^2} + G(x,t) - k_{TE}(x)n_h(x,t)n_T(x,t) \tag{2}$$

$$\frac{\partial n_T(x,t)}{\partial t} = k_{in}(x)n_e(x,t) - k_{TE}(x)n_h(x,t)n_T(x,t) \tag{3}$$

In order to consider only trapping and recombination at the surface, the rate constants $k_{in}(x)$ and $k_{TE}(x)$ are defined as step functions:

$$k_{in}(x) = \begin{cases} k_{in} & \text{for } x < x_s \\ 0 & \text{for } x > x_s \end{cases} \tag{4}$$

and

$$k_{TE}(x) = \begin{cases} k_{TE} & \text{for } x < x_s \\ 0 & \text{for } x > x_s \end{cases} \tag{5},$$

where x_s is the thickness of the region where the surface states are located.

We solved the system of equations 1 – 3 by numerical methods [1] n_e, n_h and n_T as a function of space and time. The PL trace is calculated as

$$PL(t) = \frac{k_{TE} \int_0^{x_s} p(x,t) n_T(x,t)\, dx}{I_0} \tag{6}.$$

The same set of equations was used for the TRMC experiment, using a different $G(x,t)$ term because of the different laser source. The change in photoconductance as a function of time is proportional to the charge carrier concentration and the charge mobilities, according to

$$\Delta G(t) \propto \int_0^L (n_e(x,t)\mu_e + n_h(x,t)\mu_h) dx \tag{7},$$

where L is the thickness of the sample and $\mu_{e(h)}$ is the mobility of electrons (holes), which is constant in time and space. After calculating ΔG, a convolution is applied to take into account the response time of the system (3 ns).[2]

In order to solve the system, we assumed that the mobilities of electrons and holes are equal and have a value of 100 cm^2 V^{-1} s^{-1}, similar to what reported in the literature.[3] We calculated D_e and D_h from μ_e and μ_h using the Einstein relation. For both TRPL and TRMC, the generation term has a Gaussian profile in time, with 43 ps and 3.5 ns fwhm, respectively. The spatial distribution of the charge generation has an exponential shape with a penetration depth of 180 nm. We simulated a sample with thickness $L = 1$ μm, considering the concentration of charges deeper in the bulk of the crystal to be negligible. The defect states are assumed to be distributed in a region with thickness $x_s = 10$ nm. The only free parameters of the model are k_{in} and k_{TE}. Equation 6 and 7 reproduce well the experimental data for $k_{in} = 5{\times}10^9$ s^{-1} and $k_{TE} = 1{\times}10^{-11}$ cm^{-3} s^{-1} (Figure 4b)

REFERENCES

(1)   Crank, J.; Nicolson, P. A Practical Method for Numerical Evaluation of Solutions of Partial Differential Equations of the Heat-Conduction Type. *Math. Proc. Cambridge Philos. Soc.* **1947**, *43*, 50–67.
(2)   Savenije, T. J.; Ferguson, A. J.; Kopidakis, N.; Rumbles, G. Revealing the Dynamics of Charge Carriers in Polymer:fullerene Blends Using Photoinduced Time-Resolved Microwave Conductivity. *J. Phys. Chem. C* **2013**, *117*, 24085–24103.
(3)   Shi, D.; Adinolfi, V.; Comin, R.; Yuan, M.; Alarousu, E.; Buin, A.; Chen, Y.; Hoogland, S.; Rothenberger, A.; Katsiev, K.; et al. Low Trap-State Density and Long Carrier Diffusion in Organolead Trihalide Perovskite Single Crystals. *Science.* **2015**, *347*, 519–522.